

# Synthetic LISA: Simulating Time Delay Interferometry in a Model LISA

Michele Vallisneri & J. W. Armstrong

*Jet Propulsion Laboratory, California Institute of Technology, Pasadena, CA 91109*

(Dated: 30 October 2003, Version 1.0)

Modeling efforts at GSFC and JPL are aimed at producing a detailed time-domain simulation of LISA. The simulated time series are intended to be useful in developing/validating vetos and in testing signal-processing procedures to be used on the actual data. LISA will use Time Delay Interferometry (TDI) to cancel the otherwise overwhelming laser phase noise. Here we describe the current version of a software package which produces synthetic LISA time series. This package simulates the gravitational-wave (GW) and noise responses of LISA through the TDI transfer functions. It does this for all the TDI combinations: unequal arm Michelson (X, Y, Z), Sagnac ( $\alpha, \beta, \gamma$ ), beacon (P, Q, R), monitor (E, F, G), relay (U, V, W), and symmetrical Sagnac ( $\zeta$ ). The GW signal response includes the amplitude and phase modulation of signals due to the changing geometry as the array orbits the sun.

## I. INTRODUCTION

There is an extensive effort to produce a high-fidelity model of LISA [1]. One important aspect of the mission is the overwhelmingly large laser noise which must be canceled (by about 9 orders of magnitude) so that LISA can reach its design sensitivity to gravitational waves (GWs). The procedure for laser noise cancellation is Time Delay Interferometry [2–12], TDI. This whitepaper describes the current version of a software package that emulates TDI and produces simulated time series of the GW signal and noises.

## II. TIME DELAY INTERFEROMETRY

### A. Cancellation of Raw Laser Noise

LISA seeks to observe GW signals with amplitudes that are orders of magnitude smaller than the laser noises in the array. In conventional equal-arm Michelson interferometers, the signals in the two arms are differenced on a photodetector; the laser noise is common to the two arms and it cancels, so sensitivity is dominated by the secondary noises and the signals. LISA will necessarily have unequal arms (by  $\simeq 2\%$ ); simple differencing of the arms fails, by orders of magnitude, to provide the  $\simeq 180\text{dB}$  of laser noise suppression required to reach LISA's design sensitivity.

TDI [2–12] views LISA in a symmetrical way, not only as a Michelson-type interferometer. The basic idea is to record appropriate data throughout the array and combine them with suitable time shifts to cancel all laser noises. Phase locking of the lasers in the array can be implemented, but is not required. Many laser-noise-free TDI combinations (not just the unequal-arm Michelson) can be formed simultaneously. For each TDI combination there is a different coupling to GWs and secondary noises. These multiple TDI combinations provide architectural freedom and can be useful for on-orbit instrumental noise verification, for separating the confusion-limited GW background from instrumental noise, and for contingency in the case of loss of subsystems.

For background information on TDI, see Refs. [2–12]. A general tutorial on “original TDI” is given in Ref. [10]. Reference [2] discusses the Michelson configuration in particular, and it shows why alternate laser-canceling schemes based on Fourier techniques are not practical for LISA. As discussed below, more recent TDI developments can be found in Refs. [6–8, 15, 17].

### B. TDI in Various Approximations

TDI has been developed in increasing complexity:

1. *Original TDI*. Original TDI cancels laser noise in the case of unequal arms, a rigid LISA array, and  $L_i = L'_i$  (where  $L_i$  and  $L'_i$  are the light times in the arms opposite spacecraft  $i$ , when the laser propagates in the counterclockwise and clockwise directions, respectively; see Fig. 1). Original TDI considers six lasers, six optical benches, 12 data time series (six fractional-frequency-fluctuation Doppler measurements between optical-bench pairs on different spacecraft; six fractional-frequency-fluctuation Doppler measurements between optical benches on the same spacecraft) [2–4, 9, 11, 12, 19].

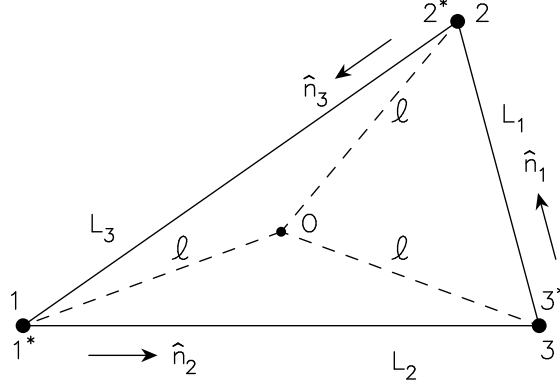


FIG. 1: Schematic LISA configuration. Each spacecraft is equidistant from the point  $O$ , in the plane of the spacecraft. Unit vectors  $\hat{n}_i$  point between spacecraft pairs with the indicated orientation. At each vertex spacecraft there are two optical benches (denoted 1, 1\*, etc.), as indicated. The armlengths  $L_i$ , measured in the counterclockwise directions, are indicated. (For generalized TDI [7, 8, 15, 17] – treated in subsequent versions of our simulations – the armlengths in the clockwise directions are  $L'_i$ .)

2. *Modified TDI*. Modified TDI cancels laser noise in the case of unequal arms, rigid array, and  $L_i \neq L'_i$  (due to aberration) [6–8]. Modified TDI is a straightforward extension of Original TDI, which will be incorporated in the next version of the simulation.
3. *Second-Generation TDI*. Second-generation TDI cancels laser noise for unequal arms,  $L_i \neq L'_i$ , and a shearing LISA array (i.e., the time delays are themselves functions of time) [7, 8, 15, 17]. Second-generation TDI will be treated in a future version of the simulation code.

### C. Notation and Conventions

In this version of the simulation, we adopt the original TDI notation and conventions (see, e.g., Refs. [4, 10]), briefly reviewed below. Figure 1 shows the overall geometry of the LISA detector. The spacecraft are labeled 1, 2, 3, and the distances between pairs of spacecraft are denoted as  $L_1, L_2, L_3$ , with  $L_i$  being opposite spacecraft  $i$ . The unit vectors between the spacecraft are denoted as  $\hat{n}_i$ , and are oriented as indicated in Figure 1. We similarly index the Doppler data to be analyzed:  $y_{31}$  is the fractional<sup>1</sup> Doppler series derived from reception at spacecraft 1 with transmission from spacecraft 2. Similarly,  $y_{21}$  is the Doppler time series derived from reception at spacecraft 1 with transmission at spacecraft 3. The other four  $y$  variables are interpreted by cyclic permutation of the indices:  $1 \rightarrow 2 \rightarrow 3 \rightarrow 1$ . We also adopt a useful notation for delayed data streams:  $y_{31,2} = y_{31}(t - L_2)$ ,  $y_{31,23} = y_{31}(t - L_2 - L_3) = y_{31,32}$ , etc. (We take  $c = 1$  throughout this paper). Six more Doppler series result from laser beams exchanged between adjacent optical benches; these are similarly indexed as  $z_{ij}$  ( $i, j = 1, 2, 3$ ).

The proof-mass-plus-optical-bench assemblies for LISA spacecraft number 1 are shown schematically in Fig. 2. We take the left-hand optical bench to be bench number 1, while the right-hand bench is 1\*. The photodetectors that generate the data  $y_{21}, y_{31}, z_{21}$ , and  $z_{31}$  at spacecraft 1 are shown. The fractional frequency fluctuations of the laser on optical bench 1 is  $C_1(t)$ ; on optical bench 1\* it is  $C_1^*(t)$ ; these are independent (the lasers need not be locked). We extend the cyclic notation of Ref. [3] in that at vertex  $i$  ( $i = 1, 2, 3$ ) the random velocities of the two proof masses are respectively denoted  $\vec{v}_i(t)$  and  $\vec{v}_i^*(t)$ , and the random velocities (perhaps several orders of magnitude greater) of their optical benches are correspondingly denoted  $\vec{V}_i(t)$  and  $\vec{V}_i^*(t)$ . (Thus, Ref. [3] considered the case  $\vec{V}_i = \vec{v}_i = \vec{V}_i^* = \vec{v}_i^*$ .) Note that the analysis of this paper does *not* assume that pairs of optical benches are rigidly connected; that is, in general  $\vec{V}_i \neq \vec{V}_i^*$ . The present LISA design shows optical fibers transmitting signals between adjacent benches. We ignore time-delay effects for these signals, and we simply denote by  $\eta_i(t)$  the frequency shifts upon transmission through the fibers (ultimately due to a component of the relative bench motions,  $\vec{V}_i - \vec{V}_i^*$ ). The  $\eta(t)$  frequency shift within a given spacecraft is the same for both local beams, positive if the benches are approaching and negative if they are separating.

<sup>1</sup> Or, equivalently, normalized by center frequency – we omit this qualifier in the rest of this paper.

The four photodetector readouts at vertex 1, including gravitational wave signals and shot noises as in [4], are thus

$$y_{21} = C_{3,2} - \hat{n}_2 \cdot \vec{V}_{3,2} + 2\hat{n}_2 \cdot \vec{v}_1^* - \hat{n}_2 \cdot \vec{V}_1^* - C_1^* + y_{21}^{\text{gw}} + y_{21}^{\text{shot}} \quad (1)$$

$$z_{21} = C_1 + 2\hat{n}_3 \cdot (\vec{v}_1 - \vec{V}_1) + \eta_1 - C_1^* \quad (2)$$

$$y_{31} = C_{2,3}^* + \hat{n}_3 \cdot \vec{V}_{2,3}^* - 2\hat{n}_3 \cdot \vec{v}_1 + \hat{n}_3 \cdot \vec{V}_1 - C_1 + y_{31}^{\text{gw}} + y_{31}^{\text{shot}} \quad (3)$$

$$z_{31} = C_1^* - 2\hat{n}_2 \cdot (\vec{v}_1^* - \vec{V}_1^*) + \eta_1 - C_1 \quad (4)$$

Eight other relations, for the readouts at vertices 2 and 3, are given by cyclic permutation of the indices in equations (1)–(4). The GW signal components in equations (1) and (3) are discussed later in Sec. III. The shot-noise contributions,  $y_{ij}^{\text{shot}}$ , due to the low signal-to-noise ratio (SNR) in the links connecting the distant spacecraft, are given in Ref. [3]. The  $z_{ij}$  measurements will be made with high SNR, so shot noise is negligible there.

The TDI data combinations that cancel the six laser noises and the noninertial motions of the optical benches are the unequal arm interferometer (X,Y,Z), Sagnac ( $\alpha, \beta, \gamma$ ), beacon (P,Q,R), monitor (E,F,G), relay (U,V,W), and symmetrical Sagnac ( $\zeta$ ) [2–4, 10]. In terms of the  $y_{ij}$  and  $z_{ij}$ ,

$$\begin{aligned} X = & y_{32,322} - y_{23,233} + y_{31,22} - y_{21,33} + y_{23,2} - y_{32,3} + y_{21} - y_{31} \\ & + \frac{1}{2}(-z_{21,2233} + z_{21,33} + z_{21,22} - z_{21}) \\ & + \frac{1}{2}(+z_{31,2233} - z_{31,33} - z_{31,22} + z_{31}) \end{aligned} \quad (5)$$

$$\begin{aligned} \alpha = & y_{21} - y_{31} + y_{13,2} - y_{12,3} + y_{32,12} - y_{23,13} \\ & - \frac{1}{2}(z_{13,2} + z_{13,13} + z_{21} + z_{21,123} + z_{32,3} + z_{32,12}) \\ & + \frac{1}{2}(z_{23,2} + z_{23,13} + z_{31} + z_{31,123} + z_{12,3} + z_{12,12}) \end{aligned} \quad (6)$$

$$\begin{aligned} P = & y_{32,2} - y_{23,3} - y_{12,2} + y_{13,3} + y_{12,13} - y_{13,12} + y_{23,311} - y_{32,211} \\ & + \frac{1}{2}(-z_{21,23} + z_{21,1123} + z_{31,23} - z_{31,1123}) \\ & + \frac{1}{2}(-z_{32,2} + z_{32,112} + z_{12,2} - z_{12,112}) \\ & + \frac{1}{2}(-z_{13,3} + z_{13,113} + z_{23,3} - z_{23,113}) \end{aligned} \quad (7)$$

$$\begin{aligned} E = & y_{12,21} - y_{13,31} - y_{12,3} + y_{13,2} + y_{31,11} - y_{21,11} - y_{31} + y_{21} \\ & - \frac{1}{2}(z_{13,2} + z_{21} + z_{32,3} - z_{13,112} + z_{23,112} - z_{32,113}) \\ & + \frac{1}{2}(z_{23,2} + z_{31} + z_{12,3} - z_{12,113} + z_{21,11} - z_{31,11}) \end{aligned} \quad (8)$$

$$\begin{aligned} U = & y_{21,113} - y_{21,3} - y_{12,123} + y_{13,1} - y_{13,23} + y_{32,11} - y_{32} + y_{12} \\ & - \frac{1}{2}(z_{31,3} + z_{12} + z_{23,23} + z_{32,11} + z_{13,1123} + z_{21,113}) \\ & + \frac{1}{2}(z_{21,3} + z_{32} + z_{13,23} + z_{12,11} + z_{23,1123} + z_{31,113}) \end{aligned} \quad (9)$$

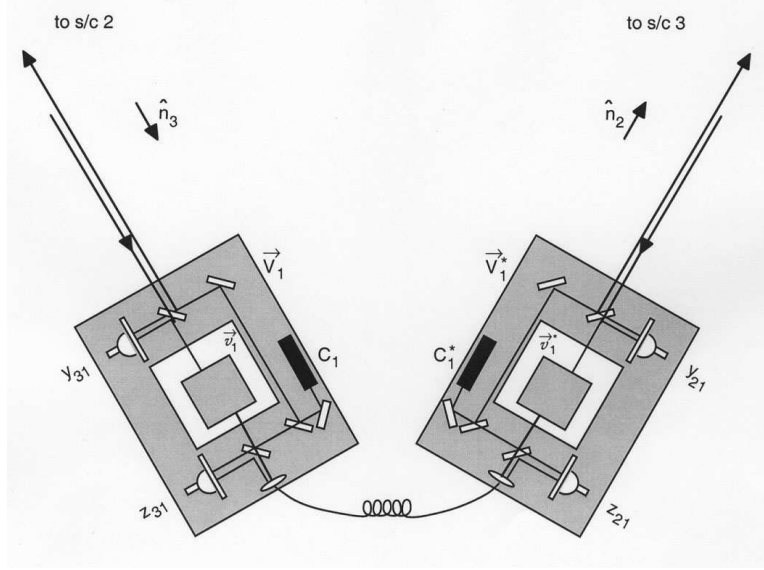


FIG. 2: Schematic diagram (adapted from Ref. [14]) of proof-masses-plus-optical-benches for a LISA spacecraft. The left-hand bench reads out the Doppler signals  $y_{31}$  (from spacecraft 2, bounced off the left proof mass, read out using laser and photodetector on the left optical bench) and  $z_{31}$  (from the right optical bench, bounced off the right-hand proof mass, redirected to the left-hand bench, and read out with the laser/photodetector on the left bench). The right hand bench analogously reads out  $y_{21}$  and  $z_{21}$ . The random velocities of the two proof masses and two optical benches are indicated (lower case  $\vec{v}_i$  for the proof masses, upper case  $\vec{V}_i$  for the optical benches.)

$$\begin{aligned} \zeta = & y_{32,2} - y_{23,3} + y_{13,3} - y_{31,1} + y_{21,1} - y_{12,2} \\ & + \frac{1}{2}(-z_{13,21} + z_{23,12} - z_{21,23} + z_{31,23} - z_{32,13} + z_{12,13}) \\ & + \frac{1}{2}(-z_{32,2} + z_{12,2} - z_{13,3} + z_{23,3} - z_{21,1} + z_{31,1}) \end{aligned} \quad (10)$$

The transfer functions for GWs and secondary noise sources (optical-path and shot noises) are given in Refs. [3, 10]. Example noise spectra are given in Refs. [4, 5, 10, 20].

### III. SIMULATION OF GRAVITATIONAL WAVE SIGNALS

We now show expressions for the GW response of the basic Doppler observables  $y_{ij}(t)$ . In the following, we set  $G = c = 1$ , and we build on the procedures and conventions of Ref. [21].

For simplicity, we start by considering a stationary constellation, at rest with respect to what we shall call the *LISA reference frame*. We define the vectors  $\vec{p}_i$  to give the position of the three spacecraft with respect to the center of the constellation; a suitable choice for an equilateral configuration is

$$\vec{p}_i = \ell \begin{pmatrix} \cos 2\pi(i-1)/3 \\ -\sin 2\pi(i-1)/3 \\ 0 \end{pmatrix}, \quad (11)$$

with  $\sqrt{3}\ell = 5 \times 10^6 \text{ km}$ . We also use the unit vectors  $\hat{n}_i \propto \epsilon_{ijk}(\vec{p}_j - \vec{p}_k)$ , which point along the links ( $\hat{n}_1$  points from spacecraft 3 to 2,  $\hat{n}_2$  from 1 to 3,  $\hat{n}_3$  from 2 to 1); here  $\epsilon_{slr}$  is the totally antisymmetric 3-D tensor. The lengths of the links are given in terms of the  $\vec{p}_i$  by  $L_i = |\epsilon_{ijk}(\vec{p}_j - \vec{p}_k)|$ .

At the position  $\vec{x}$  in the LISA frame, the spatial part of the transverse-traceless metric perturbation associated with a plane gravitational wave can be written as

$$\mathbf{h}(t) = h_+(t - \hat{k} \cdot \vec{x}) \mathbf{e}_+ + h_\times(t - \hat{k} \cdot \vec{x}) \mathbf{e}_\times : \quad (12)$$

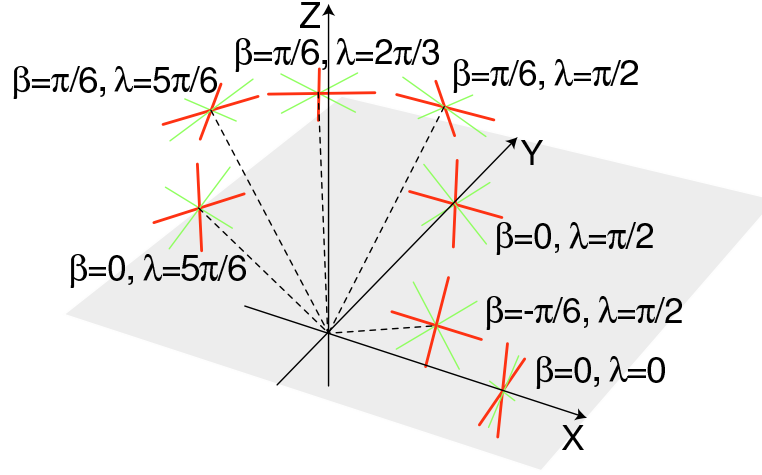


FIG. 3: GW polarizations according to the convention of Eq. (14) with  $\psi = 0$ . The heavy (red) lines denote the  $\mathbf{e}_+$  axes.

here the functions  $h_+(t)$  and  $h_\times(t)$  express the two polarization components of the wave<sup>2</sup>, referred to the origin of the LISA frame; for a GW source at latitude  $\beta$  and longitude  $\lambda$ , the unit propagation vector  $\hat{k}$  is

$$\hat{k} \equiv -(\cos \beta \cos \lambda, \cos \beta \sin \lambda, \sin \beta); \quad (13)$$

last, the two polarization tensors  $\mathbf{e}_+$  and  $\mathbf{e}_\times$  can be defined (without loss of generality) as

$$\mathbf{e}_+ \equiv \mathbf{E} \cdot \begin{pmatrix} 1 & 0 & 0 \\ 0 & -1 & 0 \\ 0 & 0 & 0 \end{pmatrix} \cdot \mathbf{E}^T, \quad \mathbf{e}_\times \equiv \mathbf{E} \cdot \begin{pmatrix} 0 & 1 & 0 \\ 1 & 0 & 0 \\ 0 & 0 & 0 \end{pmatrix} \cdot \mathbf{E}^T. \quad (14)$$

In Eq. (14), the orthogonal matrix  $\mathbf{E}$  expresses the Euler rotation sequence

$$\mathbf{E} \equiv \begin{pmatrix} \sin \lambda \cos \psi - \cos \lambda \sin \beta \sin \psi & -\sin \lambda \sin \psi - \cos \lambda \sin \beta \cos \psi & -\cos \lambda \cos \beta \\ -\cos \lambda \cos \psi - \sin \lambda \sin \beta \sin \psi & \cos \lambda \sin \psi - \sin \lambda \sin \beta \cos \psi & -\sin \lambda \cos \beta \\ \cos \beta \sin \psi & \cos \beta \cos \psi & -\sin \beta \end{pmatrix}, \quad (15)$$

where the  $\beta$  and  $\lambda$  terms can be understood as enforcing the transversality of the GW, while  $\psi = \psi(\beta, \lambda)$  is an arbitrary polarization angle. For simplicity, we take  $\psi = 0$ ; the resulting polarization directions are shown in Fig. 3.

Bringing together these ingredients, the response of the  $y_{ij}(t)$  to a plane gravitational wave is given by [22]

$$y_{lr}^{\text{gw}}(t) = y_{(s)lr}(t) = [1 + \epsilon_{slr} \hat{k} \cdot \hat{n}_l] (\Psi_l(t - \hat{k} \cdot \vec{p}_s - L_l) - \Psi_l(t - \hat{k} \cdot \vec{p}_r)), \quad (16)$$

where

$$\Psi_l(t) = \frac{\hat{n}_l \cdot \mathbf{h}(t) \cdot \hat{n}_l}{2[1 - (\hat{k} \cdot \hat{n}_l)^2]}. \quad (17)$$

According to the notation outlined in Sec. II C, the index  $r$  denotes the receiving spacecraft, the index  $l$  the transmission link, and the (implicit) index  $s$  the emitting (sending) spacecraft. The retarded responses used in the TDI combinations are obtained simply by replacing  $t$  in Eq. (16) with the appropriate retarded times. In Eq. (16), the two  $\hat{k} \cdot \vec{p}$  products correspond to the retardation of the wavefront to the position of the two spacecraft; the further delay  $L_l$  corresponds to the retardation of the wavefront to the emission event (while the reception event occurs at time  $t$ ); in Eqs. (16), (17), the  $\hat{k} \cdot \hat{n}$  products are geometrical projection factors.

<sup>2</sup> For instance, for a simple monochromatic binary one can set  $h_+(t) = A(1 + \cos^2 \iota) \cos(2\pi f t + \phi_0)$ ,  $h_\times(t) = A(2 \cos \iota) \sin(2\pi f t + \phi_0)$ , where  $\iota$  is the inclination angle,  $f$  is the GW frequency observed in the LISA frame,  $\phi_0$  is the initial phase, and  $A = (2m_1 m_2 / d R)$  is the amplitude, with  $m_1, m_2$  the two masses,  $d$  the luminosity distance,  $R$  the orbital separation.

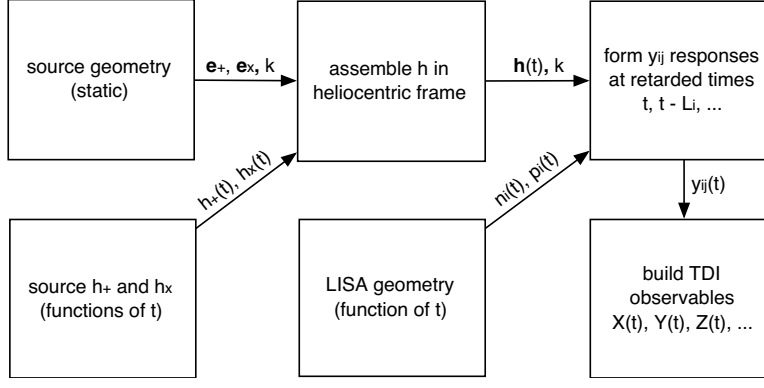


FIG. 4: Data flow for the signal part of the simulation. See text.

These expressions can be generalized to a moving LISA constellation (in the approximation of slowly moving spacecraft), by turning the  $\vec{p}_i$  (and therefore the  $\hat{n}_i$ ) into functions of time. To do this, we refer all vectors to a heliocentric, ecliptic frame where the guiding center of the LISA constellation moves in the  $(x, y)$  plane. A good approximation to the LISA trajectories, which reproduces both the solar-revolution and cartwheeling motions, but neglects the eccentricity of the orbits, is given by

$$\vec{p}_i(t) = \vec{o}(t) + \mathbf{L}(t) \cdot \vec{p}_i(0); \quad (18)$$

here  $\vec{o}(t)$  gives the motion of the LISA guiding center,

$$\vec{o}(t) = R_{\text{LISA}} \times \begin{pmatrix} \cos 2\pi(t/\text{yr}) + \eta_0 \\ \sin 2\pi(t/\text{yr}) + \eta_0 \\ 0 \end{pmatrix}, \quad (19)$$

with  $R_{\text{LISA}} = 1$  AU; the orthogonal matrix  $\mathbf{L}(t)$  expresses the Euler rotation sequence

$$\mathbf{L}(t) \equiv \begin{pmatrix} \sin \eta(t) \cos \xi(t) - \cos \eta(t) \sin \zeta \sin \xi(t) & -\sin \eta(t) \sin \xi(t) - \cos \eta(t) \sin \zeta \cos \xi(t) & -\cos \eta(t) \cos \zeta \\ -\cos \eta(t) \cos \xi(t) - \sin \eta(t) \sin \zeta \sin \xi(t) & \cos \eta(t) \sin \xi(t) - \sin \eta(t) \sin \zeta \cos \xi(t) & -\sin \eta(t) \cos \zeta \\ \cos \zeta \sin \xi(t) & \cos \zeta \cos \xi(t) & -\sin \zeta \end{pmatrix}, \quad (20)$$

with  $\zeta = -\pi/6$ ,  $\eta(t) = 2\pi(t/\text{yr}) + \eta_0$ ,  $\xi(t) = -2\pi(t/\text{yr}) + \xi_0$ . The offsets  $\eta_0$  and  $\xi_0$  are related to the initial position and alignment of the LISA constellation, and both can be taken to be zero for simplicity. The time-dependent rotation of the link vectors  $\hat{n}_i$  in Eq. (17) introduces an amplitude modulation in the responses, generating sidebands at frequency multiples of 1/yr; the time dependence of the products  $\hat{k} \cdot \vec{p}$  introduces the instantaneous Doppler shifts caused by the relative motion of the spacecraft with respect to the heliocentric ecliptic frame [to which we now refer the gravitational perturbation  $h(t)$ ].

A simple algorithm to generate the TDI observables ( $X$ ,  $\alpha$ , and so on) according to the formalism outlined above is schematized in Fig. 4, which should be interpreted as a “pull” diagram: the request of a TDI observable at time  $t$  generates several requests (in practice, C++ function calls) for retarded Doppler responses  $y_{ij}(t - \dots)$ ; each of these is assembled using the gravitational perturbation  $\mathbf{h}$  and the LISA geometry  $\hat{n}_i$ ,  $\vec{p}_i$  at specific times; the tensor  $\mathbf{h}$  is assembled using the (static) source geometry  $\hat{k}$ ,  $\mathbf{e}_+$ ,  $\mathbf{e}_\times$ , and the (time-dependent) polarization amplitudes  $h_+$  and  $h_\times$ . This algorithm is currently implemented in the signal part of the JPL LISA simulator (*Synthetic LISA*), and it has the advantage of allowing a modular structure whereby the LISA geometry and the wave amplitudes can be easily replaced with user-written functions that apply to different situations. Figures 5 and 6 show the X spectrum for a monochromatic binary with frequency  $f_0 = 2$  mHz, as produced by the algorithm described above. The X signal spectra are superimposed to a noise spectrum for X.

## IV. SIMULATION OF NOISE

### A. Overview

The noise simulation is done in steps. In the first step time series of proof-mass, optical-path, and laser noises are generated using digital filters, with user-specified spectral levels. The shapes of the proof-mass and optical-path

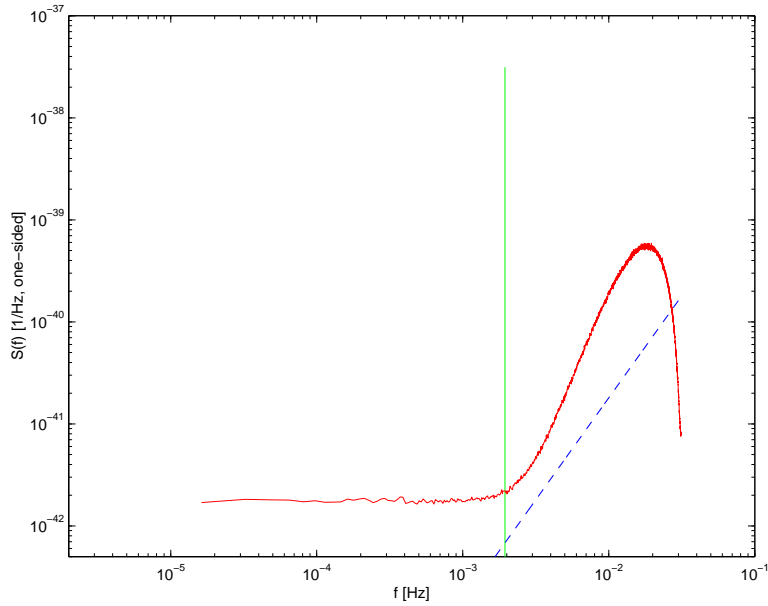


FIG. 5: Spectrum of signal in X (green) of a monochromatic binary with  $f_0 = 2$  mHz, located at zero ecliptic latitude and longitude, superimposed on an averaged noise spectrum (red) for X. Both were generated by Synthetic LISA in a year-long run with sampling time of 16 s. The (power) signal-to-noise ratio was chosen to be large, to emphasize the modulation structure of the signal (see Fig. 6). A triangle window function was used in the estimation of the spectra.

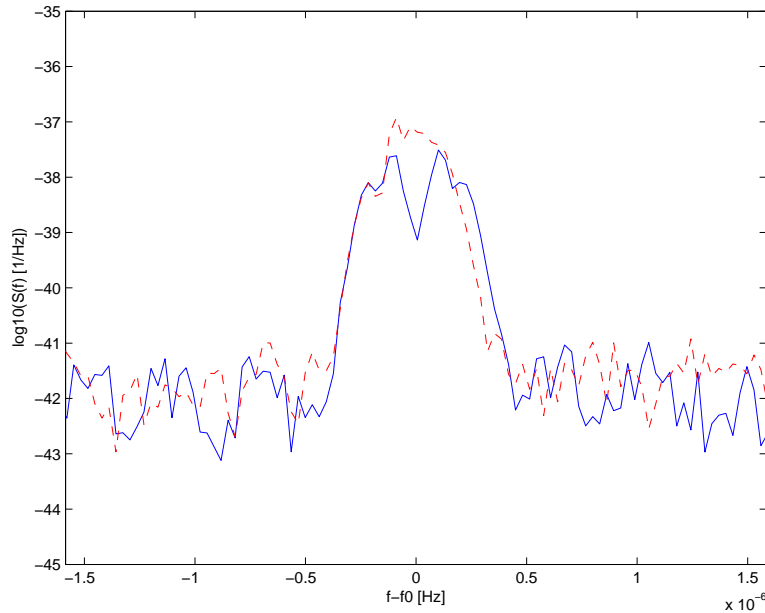


FIG. 6: Close up plot of the X spectrum, signal plus one realization of the noise, for the monochromatic binary of Fig. 5 (with  $f_0 = 2$  mHz), located at zero ecliptic latitude and longitude (blue curve), and at ecliptic latitude  $= \pi/5$ , ecliptic longitude  $= \pi/3$  (red dashed curve). The modulation structure due to the rotation of LISA's plane is evident. The spectra include noise, and they have been windowed, but not averaged.

spectra are fixed, but the level of each is under user control. From the proof-mass, laser, and optical-path time series, the observables  $y_{ij}$  and  $z_{ij}$  are generated and written to disk. If desired, these are quantized to a user-specified number of bits, to model (partially) the finite accuracy of the measurement process. Next, TDI is performed, fully in the time domain, using the definitions of the TDI combinations. The time series of the TDI combinations are written to disk, for use by other studies. The spectra of the simulated time series are measured at various points in the process, to verify fidelity of the simulation. The use of intermediate disk files is intended to modularize the

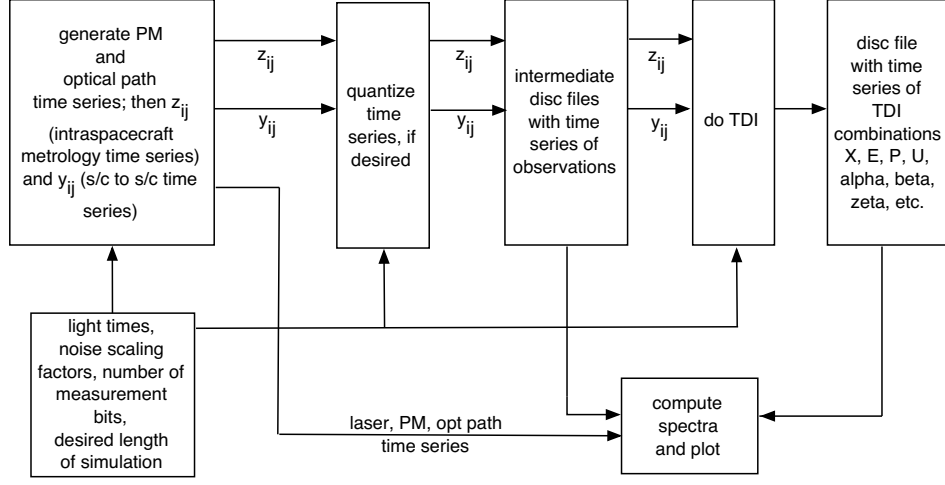


FIG. 7: Data flow for the noise part of the simulation.

process, allowing, for example, modelers to substitute their own files of simulated data (e.g., to investigate the effect of different assumptions about subsystems through the TDI process) if desired. The data flow is illustrated in Fig. 7.

## B. Generation of Laser, Proof-Mass, and Optical Path Time Series

The simulation starts with the generation of 18 time series: six for each of the laser noises (the  $C_i$  and  $C_1^*$  in Eqs. (1)–(4), six optical-path noises (sum of shot noise, pointing noise, and other optical-path noises) on the six one-way beams between optical benches on spacecraft pairs, and six proof-mass noise time series. In this version of the software, the time step is  $\Delta = 1$  second.

**Laser Noises:** The laser noises are taken to be white, and to have a one-sided (square-root) spectral density of  $30 \text{ Hz}/\sqrt{\text{Hz}}$  [13]. The laser noises  $C_i$  and  $C_1^*$  are generated as follows. Let  $n(t)$  be a white, unit-variance-Gaussian, discrete-time noise process generated by adding 12 random numbers, uniformly distributed on the interval  $(-0.5, 0.5)$ . The laser noises are produced by scaling the  $n(t)$ , so that the (square-root) frequency spectrum is  $30 \text{ Hz}/\sqrt{\text{Hz}}$ . This converts to a spectrum of  $\Delta f/f_0$  by squaring and dividing by the square of the optical frequency ( $\simeq 3 \times 10^{14} \text{ Hz}$ ). The six laser noises are generated independently, and are thus statistically independent.

**Proof-Mass Noises:** The simulated proof mass (PM) noise along the sensitive axis is generated by a digital filter:  $x^{\text{proof mass}}(t) = \alpha x^{\text{proof mass}}(t - \Delta) + n(t)$ . The Fourier transform gives the transfer function:  $\hat{x}^{\text{proof mass}}(f)(1 - \alpha e^{-2\pi i f \Delta}) = \hat{n}(f)$ . Thus the spectrum of  $x^{\text{proof mass}}$  will be related to the white spectrum of  $n(t)$  by the spectral transfer function:  $|1/(1 - \alpha \exp(2\pi i f \Delta))|^2$ . The output is scaled to give the expected PM spectral level in the LISA band. From Ref. [13], Table 4.2, the acceleration noise spectrum of a single proof mass is  $3 \times 10^{-15} \text{ m sec}^{-2} \text{ Hz}^{-1/2}$ . To convert to a spectrum of fractional frequency fluctuations [10], we use the derivative theorem for Fourier transforms, and note that dividing the velocity spectrum by the speed of light squared gives the power spectrum of fractional frequency fluctuations:  $S_y^{\text{proof mass}} = (3 \times 10^{-15} \text{ m sec}^{-2} \text{ Hz}^{-1/2})^2 / (4\pi^2 f^2 c^2) = 2.5 \times 10^{-48} [f/1\text{Hz}]^{-2} \text{ Hz}^{-1}$ . We take  $\alpha = 0.9999$ ,  $\Delta = 1$  and scale the output of the digital filter (in the nominal case—variations in level are under user control) to have the one-sided spectrum given above. Figure 8 shows the one-sided power spectrum of the proof mass noise thus generated, compared to the desired spectrum  $2.5 \times 10^{-48} [f/1\text{Hz}]^{-2} \text{ Hz}^{-1}$  (dashed line).

**Optical-Path Noise:** The shot-noise spectrum for an individual laser link is given in the Pre-Phase A Study [13], Table 4.2. Here we combine the shot noise and the beam-pointing noise into an aggregate optical-path noise having (square root) spectrum  $20 \times 10^{-12} \text{ m Hz}^{-1/2}$ . We assume that this aggregate optical-path noise has the same transfer function as pure shot noise. Again using the derivative theorem for Fourier transforms,  $20 \times 10^{-12} \text{ m Hz}^{-1/2}$  converts to a spectrum of velocity:  $(20 \times 10^{-12} \text{ m Hz}^{-1/2})^2 \times 4\pi^2 f^2$ . Dividing by the speed of light squared gives the power spectrum of fractional frequency fluctuations associated with optical path noise:  $S_y^{\text{optical path}} = 1.8 \times 10^{-37} (f/1 \text{ Hz})^2 \text{ Hz}^{-1}$ . Overall spectral level is under user control if a non-standard optical-path noise is desired. The  $f^2$  dependence makes an approximate implementation with digital filters easy:  $x^{\text{opt path}}(t) = n(t) - n(t - \Delta)$ , scaled to get the right



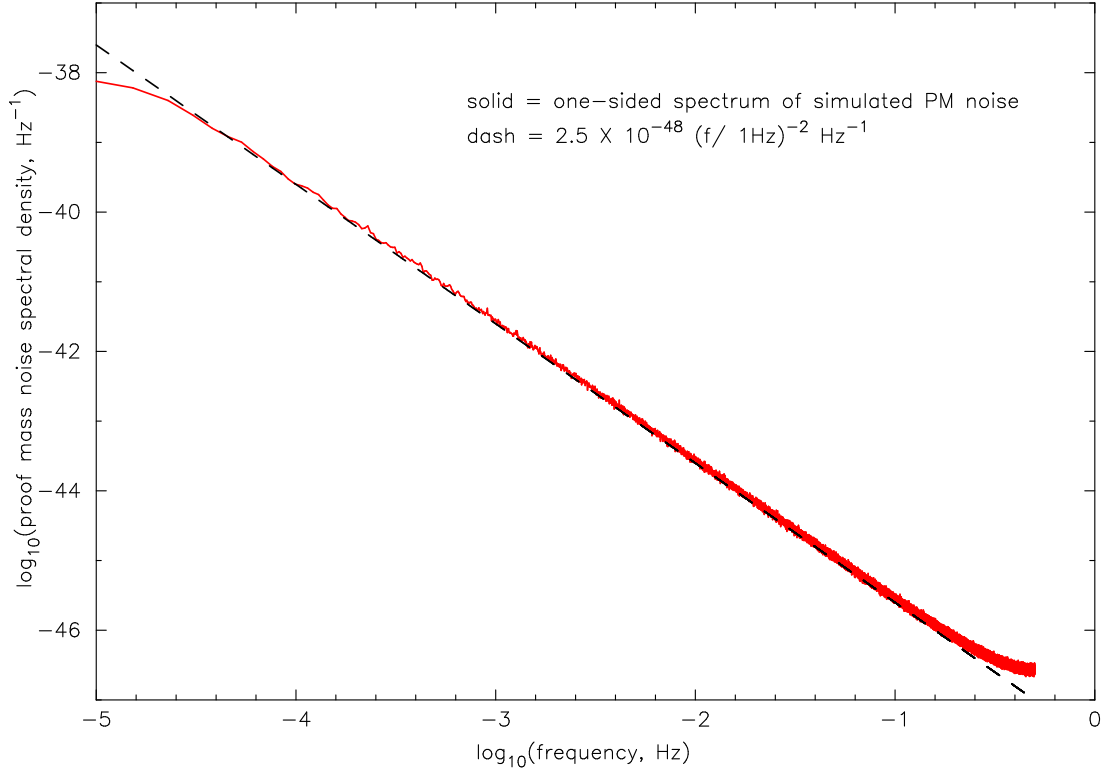


FIG. 8: Spectrum of one proof mass, computed from  $2^{25}$  seconds of simulated data according to the digital filter of the text. Solid line = spectrum of simulated data; dotted line = model spectrum.

spectrum in the low-frequency region where LISA will be most sensitive<sup>3</sup>. To account for loss in the arm lengths, the overall optical-path rms noise is scaled by  $L_i/(16.67\text{s})$  on each of the links.

### C. Generation and Verification of Noise Time Series

From Eqs. (1)–(4), we take the optical fiber noise to be zero and the bench motions to be zero (the latter, like laser noise, are algebraically canceled by TDI but could be included in future versions to explore effects of measurement and quantization noise). Given the 18 time series (six laser noise, six proof mass noises  $pm_i$  and  $pm_i^*$ , and six optical path noises  $y_{ij}^{\text{opt path}}$ ), the  $y_{ij}$ ,  $z_{ij}$  are generated from

$$y_{21} = C_{3,2} + 2pm_1^* - C_1^* + y_{21}^{\text{opt path}} \quad (21)$$

$$z_{21} = C_1 + 2pm_1 - C_1^* \quad (22)$$

$$y_{31} = C_{2,3}^* - 2pm_1 - C_1 + y_{31}^{\text{opt path}} \quad (23)$$

<sup>3</sup> The first-difference filter has a spectral transfer function proportional to  $\sin^2(\pi f \Delta)$ , so is only accurately proportional to  $f^2$  at low-frequencies; near the Nyquist frequency, 0.5 Hz, an error will be incurred. This is negligible for current use of the simulator. However, if desired, the code could be straightforwardly modified to extend the  $f^2$  dependence to 0.5 Hz by, e.g., differencing a time series sampled at 10 Hz, low pass filtering at 0.5 Hz (to avoid aliasing), and then decimating to  $\Delta = 1$  sec. For present purposes, the procedure described in the text is adequate.

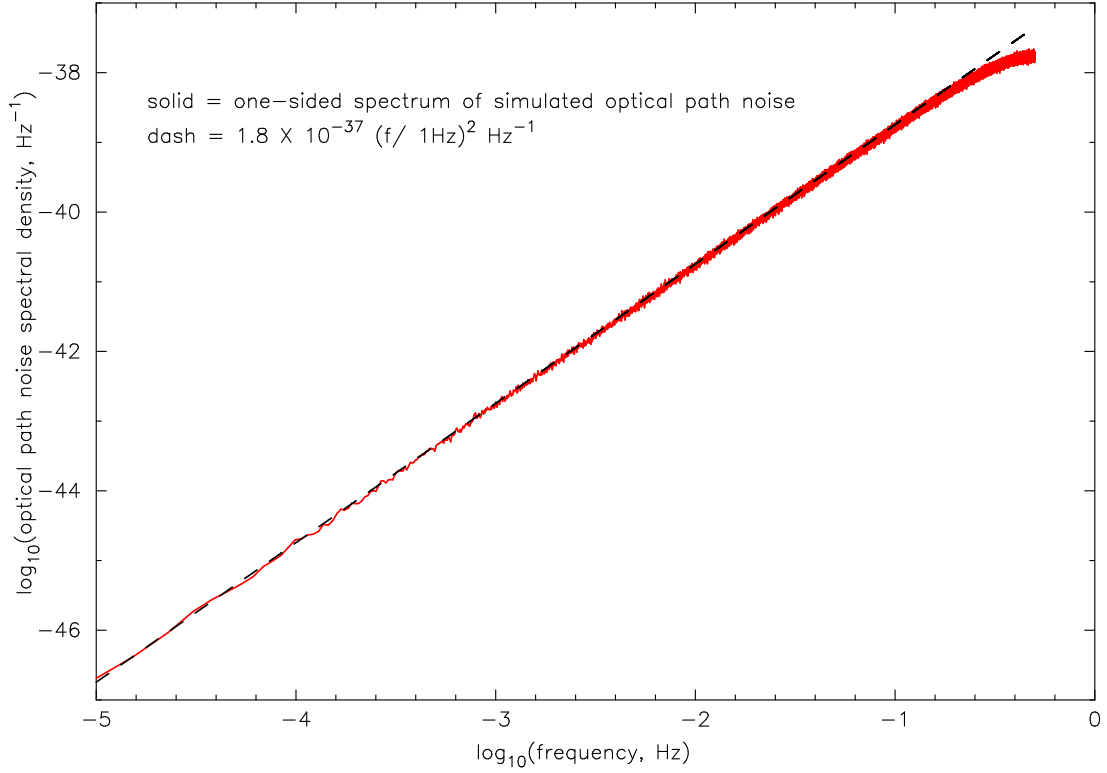


FIG. 9: Spectrum of noise on optical path, computed from  $2^{25}$  seconds of simulated data according to the difference equation in the text. Solid line = spectrum of simulated data; dotted line = model spectrum.

$$z_{31} = C_1^* - 2pm_1^* - C_1 \quad (24)$$

Eight other relations, for the readouts at vertices 2 and 3, are given by cyclic permutation of the indices. The computations are done in double precision. These 12 time series are written to disk as intermediate files.

#### D. Measurement Error

Measurement error, if it is simple white phase noise error, can be easily added in the simulation. This is done by adjusting the user-defined scale factors for the optical path noise. To get the nominal optical-path noise (aggregate optical path noise of  $20 \times 10^{-12} \text{ m Hz}^{-1/2}$ ), the scale factor for each optical path is set to unity. If, for example, one wanted to model additive measurement noise on a particular link, the scale factor for that link could be set to a number greater than unity (e.g., 1.1 if one wanted 10% larger rms noise on that link.) Each link can be adjusted independently, if desired. Additionally, if desired, the  $y_{ij}$  and  $z_{ij}$  can then be quantized to a fixed bit-depth (see Figure 7). This is to model, very crudely, one aspect of the fidelity of the measurement process. Currently this is done naively: all time series are quantized to the same bit depth, and it is assumed that the effective gain of all digitization processors in the LISA array is the same.

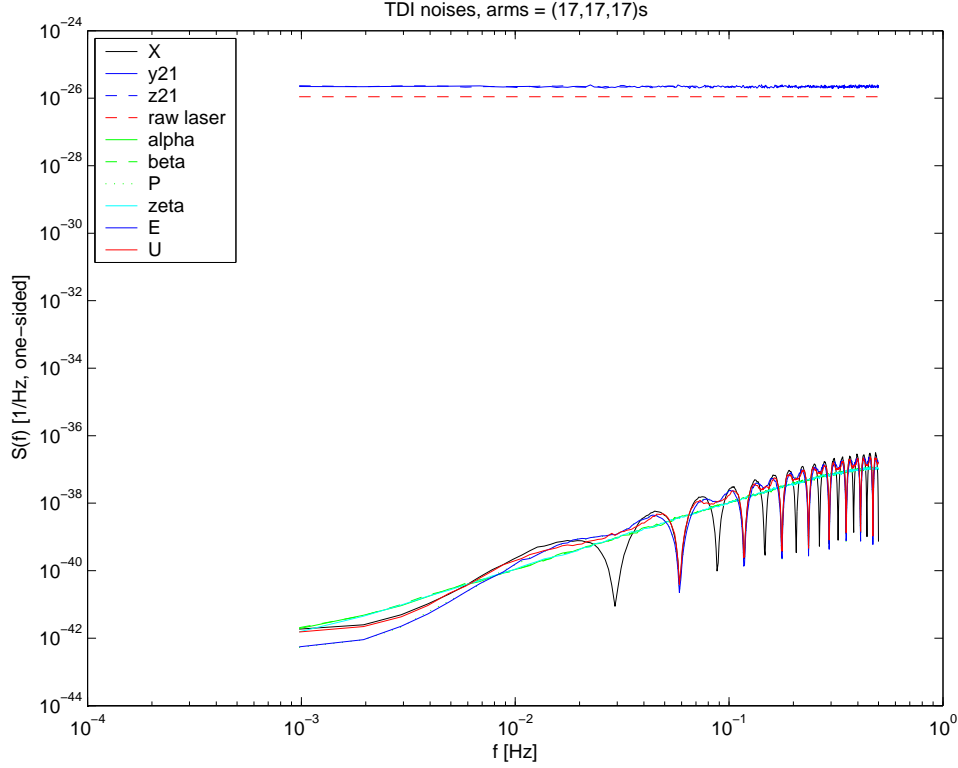


FIG. 10: Spectra of raw laser noise, the measured quantities  $y_{ij}$ ,  $z_{ij}$ , and TDI combinations  $X$ ,  $\alpha$ ,  $\beta$ ,  $P$ ,  $U$ ,  $E$ ,  $\zeta$  from a simulation run. Parameters: data length  $2^{18}$  seconds, 1 sample/second,  $L_1 = L_2 = L_3 = 17$  seconds, laser noise at  $30 \text{ Hz/Hz}^{1/2}$ . (The plotted spectra were estimated by averaging spectra of subsets of the data; the resulting resolution bandwidth causes the sharp nulls in some TDI combinations, e.g.  $X$ , to be partially filled in.) TDI cancels the laser noise, to below the level of the secondary noises (optical path and proof mass noises), i.e., by more than 180dB.

### E. Implementing TDI

We implement TDI purely in the time domain, using time-offset sums of the laser noise, proof mass noise, and optical path noise<sup>4</sup>. Equations (5)–(10) – the time-domain definitions of the TDI combinations – are directly implemented in the code and the resulting TDI time series for  $X$ ,  $Y$ ,  $Z$ ,  $\alpha$ ,  $\beta$ ,  $\gamma$ ,  $U$ ,  $\zeta$ ,  $\dots$ , are then written to disk.

Figure 10 shows an example of the spectra of the raw observables  $y_{ij}$  and  $z_{ij}$  at the top of the frame. These are dominated by the laser noises. After TDI, the laser noise has been removed and the spectra of the TDI combinations are set by proof mass and optical path noises. Figure 11 shows another simulation output, this time with unequal arm lengths. Again TDI cancels the laser noise. Spectra of the noise in the TDI combinations now have different shapes (since the light times are not all equal), but in agreement with the transfer functions for the noises (implicit in the above equations for the TDI observables; see also Refs. [4, 10]).

### F. Spectra of TDI Combinations

As one test of the output, we verify that the spectra of the laser noise, the  $y_{ij}$ , the  $z_{ij}$ , and the TDI combinations are as expected. To do this, we take the time series, divide them up into power-of-2 blocks that are short compared with the duration of the simulation, window sections with a triangle function to reduce spectral leakage and to produce high-fidelity spectra (particularly at low-frequencies [16]), and average the squared Fourier transform of the windowed blocks. The spectra we form this way are in agreement with analytical results [10]. Figure 12 shows a comparison of

<sup>4</sup> We took  $V_i = V_i^* = 0$  in these simulations. These optical bench noises cancel algebraically but could be included in subsequent versions of the simulation.

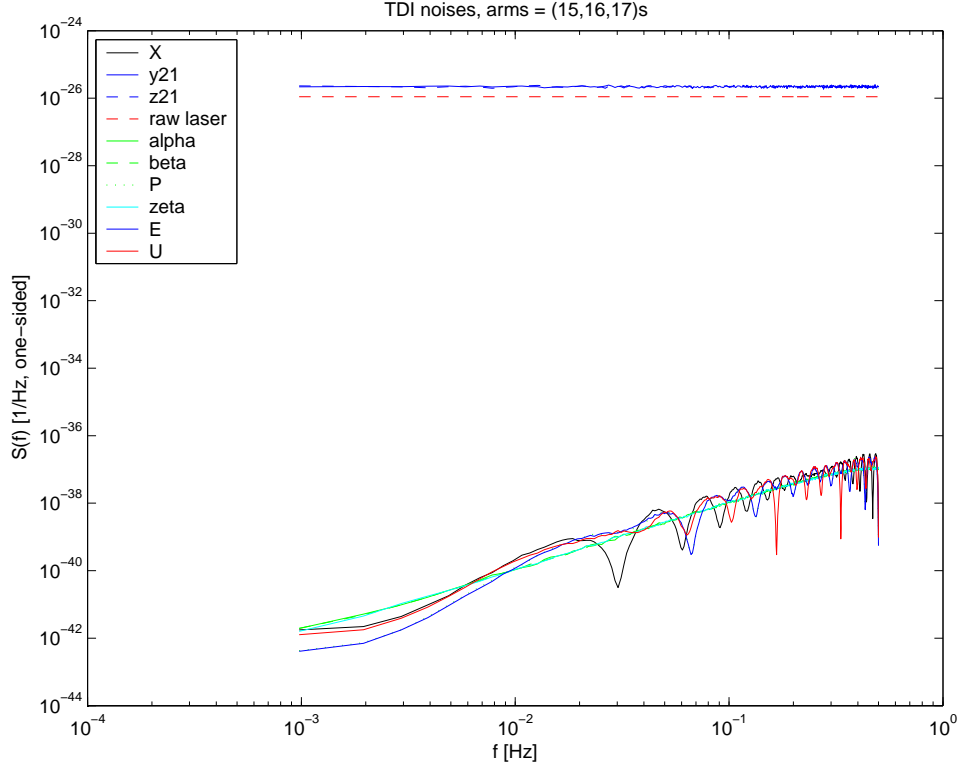


FIG. 11: As Fig. 10, but for the unequal arm case  $L_1 = 15$  sec,  $L_2 = 16$  sec,  $L_3 = 17$  sec.

the simulation output for the unequal arm Michelson combination along with the analytical spectrum for the nominal noises. The laser noise has been canceled and the spectrum of the TDI X time series is in excellent agreement with the expected spectrum of the secondary noise sources.

There are some potential subtleties in the use of the noise code and in the interpretation of the results.

1. *Geometrical Knowledge.* LISA needs to know its own geometry to know when to take the samples. In this version, the armlengths can be unequal, but are fixed, so the geometry is not changing. In a more realistic simulation the models of the subsystems cannot be developed as completely independent of the time-dependent geometry. We plan to address this in a future version of the simulator.
2. *Measurement Error.* Measurement error is currently modeled only by allowing more (white phase) noise on the optical path links through the scaling factors discussed above, and as quantization error. Different models of the measurement process could be incorporated by user-written modules that rewrite the  $y_{ij}$  and  $z_{ij}$  disk files. This would be transparent to the subsequent modules that implement TDI, and so on.
3. *Incorporating Subsystem Models.* In addition to measurement error, there may be systematic effects of the measurement process that could be investigated. Better models of subsystems can be incorporated, again by replacing the files of the  $y_{ij}$  and  $z_{ij}$  with time series that have been generated by a detailed model of the apparatus.

### G. Applications and Examples

Synthetic LISA is intended to produce time series useful in study of high-level LISA performance, development of system diagnostics and veto signals, and in the design of signal analysis procedures.

1. *Trade-Off Studies.* Synthetic time series supplement analytical results in allocation of subsystem noise budgets and in the determination of final sensitivity.
2. *Noise Analysis and Vetos.* Synthetic time series can be used to model the noises, including the nonstationarity or isolation of faulty subsystems. As a very simple example, Figure 13 shows the power spectrum of the three

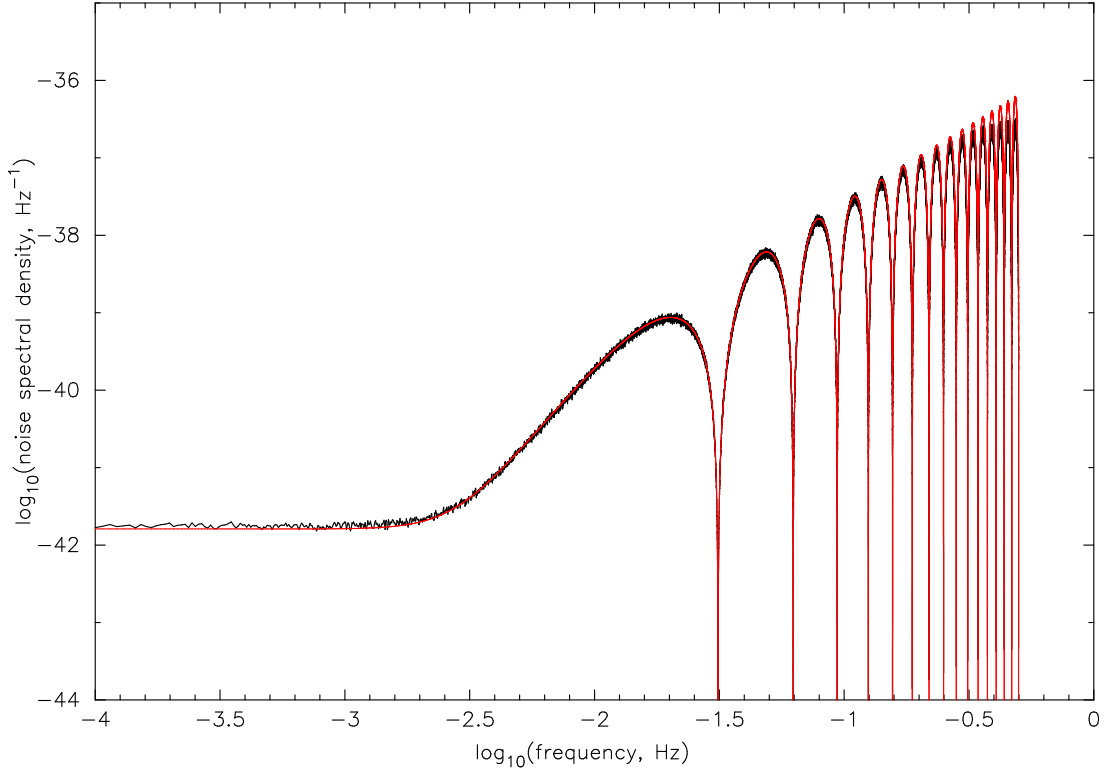


FIG. 12: Comparison of the spectrum of TDI X data combination from the simulation (black line) with expected spectrum (red line). Parameters:  $2^{25}$  seconds of simulated data,  $L_1 = L_2 = L_3 = L = 16$  seconds,  $30 \text{ Hz}/\sqrt{\text{Hz}}$  for the raw laser noise,  $3 \times 10^{-15} \text{ m/sec}^2/\sqrt{\text{Hz}}$  for the proof mass noise,  $20 \times 10^{-12} \text{ m} (L/16.67 \text{ sec})/\sqrt{\text{Hz}}$  for aggregate optical path (shot noise, beam-pointing noise, etc.) noise spectra (see text). Triangle window function was used in estimation of the spectra. The nulls on the right are deeper with respect to Figs. 10 and 11 because the longer simulation time reduces the averaging of frequency bins.

unequal-arm Michelson TDI combinations (X, Y, Z) when all noises are nominal *except* that proof mass 1 has  $10\times$  larger rms noise. Since proof mass 1 enters only in X and Z, the isolation of the problem to proof mass 1 is obvious.

3. *Optimum Combination of LISA Data and Sensitivity Verification.* Optimum sensitivity of LISA requires using all the data in the array [18]. Synthetic data can be used to supplement analytic results under simulated conditions which model potential real-LISA effects (nonstationarity of noises, data gaps, etc.)
4. *Synthetic Time Series for Algorithm Development.* The synthetic time series produced by this simulation have consistent signal structure and noise correlations across all the TDI combinations. Thus they can be used to test algorithms for use on the real LISA data, including separation of GW background from LISA Instrumental noises, matched filtering for bursts and orbit-modulated periodic waves, etc.

## H. Limitations of the Current Noise Code

The current noise code has these limitations:

1. *Arm Length Quantization.* The code currently requires arm lengths to be integer multiples of one second. For our current proof-of-concept code, this was adopted for ease of programming, and to keep the arrays at reasonable sizes. We intend to relax this in future versions.
2. *USO Noise Calibration.* The additional time series required for calibration of the ultra-stable oscillator (USO) [9], are not included in this version of the simulation.
3. *Aberration.* Owing to aberration, the real LISA will have different light times on the upleg and downleg of a given arm [6–8, 15]. This is accounted for in the Modified TDI combinations [7, 17], which will be incorporated

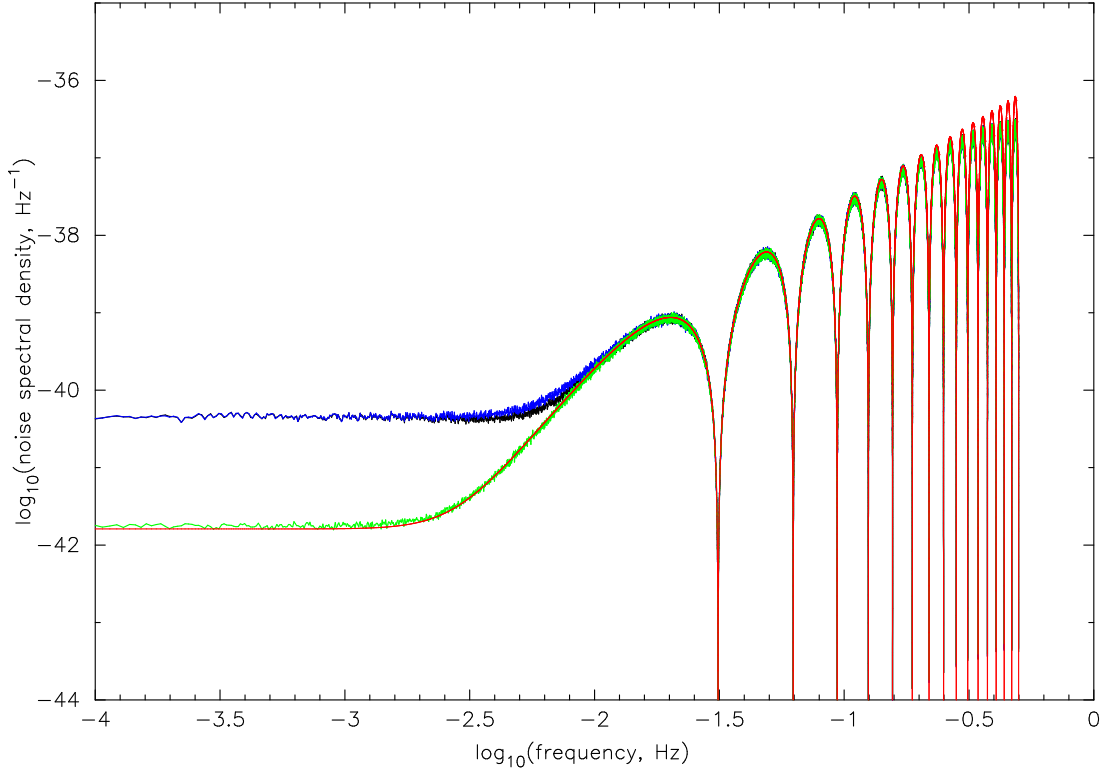


FIG. 13: Spectra of TDI combinations X, Y, and Z from a simulation where all noises are nominal, except that proof mass 1 (on spacecraft 1, facing spacecraft 2) has  $10\times$  larger rms noise. Black and blue lines are X and Y; these are degraded at low frequency due to noisier PM1 (a 20 dB noisier PM1 increases the Michelson TDI combination by  $\simeq 14.2$  dB at low frequency, when all other noises are nominal). Green line is Z; PM1 does not contribute to this TDI combination, so noise performance is nominal. Parameters:  $2^{25}$  seconds of simulated data,  $L_1 = L_2 = L_3 = L = 16$  seconds, A triangle window function was used in estimation of the spectra. Red curve is the expected spectrum for nominal proof mass and optical path noises. The nulls on the right are deeper with respect to Figs. 10 and 11 because the longer simulation time reduces the averaging of frequency bins.

in the next version of the simulation. This limitation also means that the noise model is currently independent of the geometry (e.g., rotation of the array, flexing of the array, revolution of the array around the sun). This uncoupling of the geometry – which defines when TDI samples must be taken, for example – will be addressed in future versions of the software.

4. *Secondary Noise Spectral Shapes.* The current version produces time series by running a white-noise time series through digital filters to get proof mass and optical path time series that have the expected spectral shape. We allow a user-specified scaling factor to change the level of the secondary noises (by just multiplying the time series up or down to simulate, say, a noisier or quieter proof mass). If a different shape of the spectrum were desired, it would have to be incorporated by an external program that overwrote the appropriate optical-path or proof mass data.
5. *Measurement Error.* Currently measurement error in the time series is modeled only as additive phase noise, through the scaling factors of the optical path noises and through the capability to quantize the data time series  $y_{ij}$  and  $z_{ij}$  to a fixed number of bits. As discussed above, more sophisticated models of the measurement could be done with user-defined modules prior to the TDI step.
6. *Shearing of the LISA Array.* The current version does not address the fact that the real LISA light-times will not be constant, but rather functions of time. Second-generation TDI [7, 17], to be included in a future version of the programs, solves this. Alternatively, improvements in the laser noise by factors of  $\sim 10$  would make this effect small enough to ignore. In this case the simpler Modified TDI would be sufficient for LISA.

## V. SUMMARY

We have described the current version of *Synthetic LISA*, a software package that produces time series of simulated LISA signals and noises, including their TDI processing. Laser noise is included in the simulation and is shown to cancel explicitly, using TDI, in both equal and unequal armlength configurations. The package produces signal-plus-noise series for all the TDI combinations: unequal arm Michelson (X, Y, Z), Sagnac ( $\alpha, \beta, \gamma$ ), beacon (P, Q, R), monitor (E, F, G), relay (U, V, W), and symmetrical Sagnac ( $\zeta$ ). We have shown examples of spectra of the code output; we have discussed the limitations of the current model, and our plans for generalizing it in future versions.

## APPENDIX A: COMPARISON OF LOW-FREQUENCY NOISE SPECTRA

Here we compare the noise-only spectra of TDI combination X (the unequal arm Michelson) for our simulation and a previously published simulation code by the Montana group [23]. The simulations make the same default assumption about the spectrum of proof-mass noise, but different default assumptions about the level of the optical-path/shot noises. These differences in default settings amount to a factor of four difference in power spectrum at frequencies larger than about  $10^{-3}$  Hz. However, when we match assumptions for the optical-path/shot noise, we find good agreement between the low-frequency noise-only spectra of X.

The noises are:

1. *Raw Laser Noise.* Our simulation explicitly includes raw laser noise at the nominal LISA value of  $30 \text{ Hz}/\sqrt{\text{Hz}}$ , which converts to a power spectrum of fractional frequency fluctuations of  $(30 \text{ Hz}/\sqrt{\text{Hz}})^2/(3 \times 10^{14} \text{ Hz})^2 = S_y^{\text{laser}} = 10^{-26} \text{ Hz}^{-1}$  (see indicated line in, e.g., Figure 10). Our noise simulation code shows how the laser noise is explicitly canceled (see, e.g., Figure 10) in the construction of the TDI combinations. Knowing that the laser noise must cancel algebraically, [23] omits laser noise from the current version of the simulation.
2. *Proof Mass Noise.* Both the modeling efforts start with the same value for the acceleration noise of the proof masses:  $3 \times 10^{-15} \text{ m/sec}^2/\sqrt{\text{Hz}}$ . This value can be mapped to the power spectrum of fractional frequency fluctuations of [10] using the derivative theorem for Fourier transforms and dividing the velocity spectrum by the speed of light squared:  $S_y^{\text{proof mass}} = (3 \times 10^{-15} \text{ m sec}^{-2} \text{ Hz}^{-1/2})^2/(4\pi^2 f^2 c^2) = 2.5 \times 10^{-48} [f/1 \text{ Hz}]^{-2} \text{ Hz}^{-1}$ .
3. *Shot and Optical Path Noises.* Reference [23] uses shot noise only while we attempt to account approximately for both shot noise and beam-pointing noise. Reference [23] uses  $1.0 \times 10^{-11} \text{ m}/\sqrt{\text{Hz}}$  as the shot noise on an individual link. We combine the shot noise and the beam-pointing noise into an aggregate optical-path noise having spectrum  $20 \times 10^{-12} \text{ m Hz}^{-1/2}$  [10]. As in most prior sensitivity studies ([10] and references therein) we assume that this aggregate optical path noise has the same transfer function as pure shot noise. Again using the derivative theorem for Fourier transforms,  $20 \times 10^{-12} \text{ m Hz}^{-1/2}$  converts to a velocity spectrum of  $(20 \times 10^{-12} \text{ m Hz}^{-1/2})^2 \times 4\pi^2 f^2$ . Dividing by the speed of light squared gives the power spectrum of fractional frequency fluctuations associated with optical path noise:  $S_y^{\text{optical path}} = 1.8 \times 10^{-37} (f/1 \text{ Hz})^2 \text{ Hz}^{-1}$ . Thus our simulation and [23] have default high-frequency noise levels that differ (by assumption) in spectral level by a factor of 4, ours being larger.

Analytical transfer functions for gravitational waves and secondary noise sources (optical path and shot noises) are given in [3, 10]. Example noise spectra are given above and in [4, 5, 10, 20]. In addition to the differences in the default optical-path-shot-noise level, other differences between the noise simulations are: (i) [23] produces the three unequal-arm Michelson combinations (X, Y, Z) [2–4, 10, 23]; ours produces these plus other TDI combinations (e. g., the Sagnac, symmetrical Sagnac, Michelson, beacon, relay, monitor, etc. [4, 10]); (ii) the simulation described in this whitepaper includes explicitly the intra-spacecraft calibration data (the  $z_{ij}$ , see [4]); (iii) the simulation described here includes explicitly laser-phase noise to demonstrate its cancellation in the TDI process.

The noise simulation described in this white paper starts with the generation of 18 time series: six for each of the laser noises, six optical-path noises (sum of shot noise, pointing noise, and other optical-path noises) on the six one-way beams between optical benches on spacecraft pairs, and six proof-mass-noise time series. In the noise part of our simulation the time step is  $\Delta = 1$  second and the current version of the code allows the arms to be unequal integer multiples of 1 second. The laser noises are taken to be white and have one-sided spectral density of  $30 \text{ Hz}/\sqrt{\text{Hz}}$  [13]. They are generated as follows. Let  $n(t)$  be a white, unit-variance-Gaussian, discrete-time noise process generated by adding 12 uniformly distributed random numbers in the interval  $(-0.5, 0.5)$ . The laser noises are produced by scaled versions of the  $n(t)$ , such that the fractional frequency spectrum is  $10^{-26} \text{ Hz}^{-1}$ . The six laser noises are generated independently and are thus statistically independent. In [23] the laser noise is not explicitly modeled, since TDI guarantees that it will cancel if the arm lengths are known accurately enough.

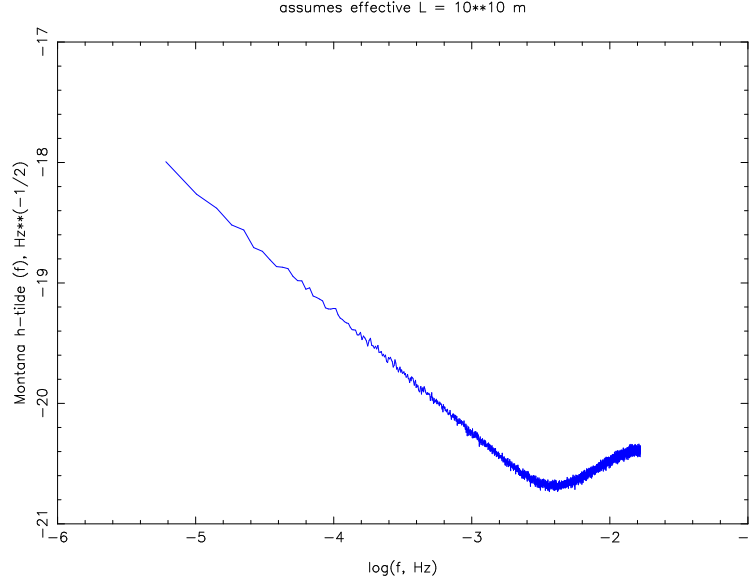


FIG. 14: A spectrum of strain for TDI combination X, as produced by the simulation code [23]; see text.

The secondary-noise spectra can be used to get the power spectrum of the TDI combinations. For example, assuming equal arm lengths,  $L$ , the spectrum of TDI X is related to the spectra of fractional frequency noises in the proof mass and the optical-path processes by [4, 10]:

$$S_X(f) = [8 \sin^2(4\pi f L) + 32 \sin^2(2\pi f L)] S_y^{\text{proof mass}} + 16 \sin^2(2\pi f L) S_y^{\text{optical path}} \quad (\text{A1})$$

To compare our spectra with those generated by [23], we convert the strain spectrum output by [23] to a spectrum of fractional frequency fluctuations as follows:

1. According to [23], the spectra produced are those of strain, assuming an effective arm length of  $10^{10}$  m. The units are  $\text{Hz}^{-1/2}$ .
2. We multiply the strain spectrum by the assumed [23] effective arm length,  $10^{10}\text{m}$ , to get a spectrum of displacement in units of  $\text{m Hz}^{-1/2}$ .
3. We then square to get the power spectrum of displacement in units of  $\text{m}^2 \text{Hz}^{-1}$ .
4. We convert to the spectrum of velocity, using the derivative theorem for Fourier transforms, by multiplying by  $4\pi^2 f^2$ . The units are  $(\text{m/sec})^2 \text{Hz}^{-1}$ .
5. We convert to a spectrum of fractional frequency fluctuations by dividing by the speed of light squared. The spectrum now has units of  $\text{Hz}^{-1}$ .
6. We finally overplot the expected spectrum,  $S_X(f)$  above, using the assumed optical path noise from [4, 10] and (with the dashed line) an optical path spectrum level that is four times lower (i. e., shot noise only, as used in [23]).

Figure 14 shows the spectrum of TDI X from the simulation of [23], expressed as strain per square-root Hz. The total simulation time was 1 year, and time between samples was  $1 \text{ year}/(2^{20}) \simeq 30.1$  seconds (i. e., the Nyquist frequency was about 0.0166 Hz). Figure 15 shows the spectrum of Figure 14 converted to fractional frequency fluctuations according to the above prescription. The red curve is the expected spectrum using the proof-mass and default optical-path spectra of [10], with equal arms ( $L = 16.67$  seconds). The red dashed curve is the expected spectrum using the assumption of [23] for the optical-path spectrum. Similar plots for TDI X spectra in our simulation are shown in the main text and agree very well with the solid red curve.

In summary: We compared low-frequency noise spectra of the TDI combination X for the two simulation codes. The [23] work produces a spectrum of strain. This spectrum was converted to a spectrum of fractional frequency fluctuations to compare with our noise spectra. The agreement at low frequencies, where the proof mass noise dominates,



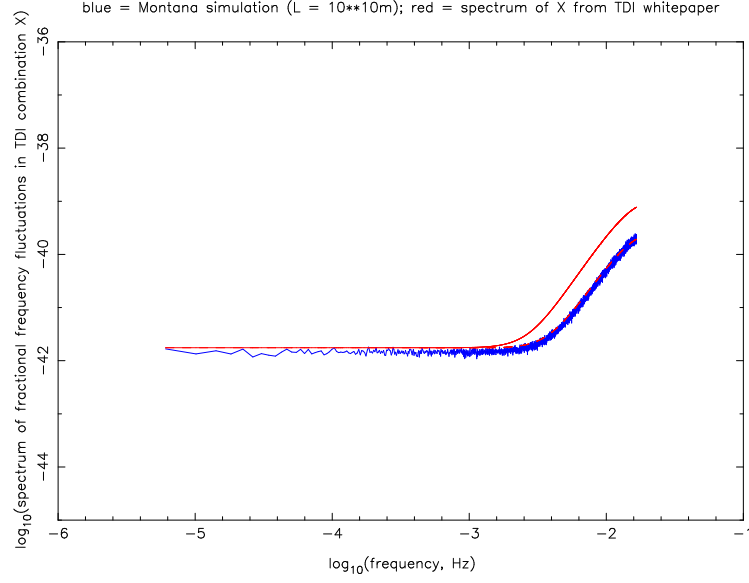


FIG. 15: Spectrum of TDI combination X from Figure 14, as produced by the simulation code [23], converted to a spectrum of fractional frequency fluctuations and compared with the analytical expectation. Blue = simulation from [23]; red = expected values using the our default optical path noise [10, 20] ; dashed red = expected values with optical path noise using the value assumed by [23].  $L = 16.67$  seconds assumed. The spectrum of X from the our code is in excellent agreement with the expected spectrum (red line). See main text.

is very good (both simulations use  $3 \times 10^{-15} \text{ m/sec}^2/\sqrt{\text{Hz}}$  for the proof-mass noise spectrum). At higher frequencies (greater than about  $10^{-3} \text{ Hz}$ , there is a systematic difference in spectral level of a factor of 4. This systematic difference simply reflects different default assumptions about the high-frequency noise in the two simulations and is understood: [23] uses a shot-noise-only spectrum whereas use four times the shot noise spectrum to approximately account for all optical path noise variations (e. g., beam pointing noise as well as shot noise).

- 
- [1] Merkowitz, S. *Classical Quantum Grav.* **20**, S255, (2003)
  - [2] Tinto, M. & Armstrong, J. W., *Phys. Rev. D*, **59**, 102003 (1999)
  - [3] Armstrong, J. W., Estabrook, F. B., & Tinto, M. *Ap. J.*, **527**, 814 (1999)
  - [4] Estabrook, F. B., Tinto, M., & Armstrong, J. W. *Phys. Rev. D*, **62**, 042002 (2000).
  - [5] Armstrong, J. W., Estabrook, F. B., & Tinto, M. *Classical Quantum Grav.*, **18**, 4049 (2001)
  - [6] Shaddock, D. A. *Phys. Rev. D* in press (2003) (gr-qc/0306125)
  - [7] Shaddock, D. A., Tinto, M., Estabrook, F. B., & Armstrong, J. W. 2003 accepted for publication in *Phys. Rev. D*, (gr-qc/030708v1)
  - [8] Cornish, N. J. and Hellings, R. W. (2003) (gr-qc/0306096).
  - [9] Tinto, M., Estabrook, F. B., & Armstrong, J. W. *Phys. Rev. D*, **65**, 082003 (2002).
  - [10] Tinto, M., Estabrook, F. B., & Armstrong, J. W. *Time Delay Interferometry White Paper*, May 15, 2002. Web posted at [http://www.srl.caltech.edu/lisa/tdi\\_wp](http://www.srl.caltech.edu/lisa/tdi_wp)
  - [11] Dhurandhar, S. V., Nayak, K. R., & Vinet, J.-Y. *Phys. Rev. D*, **65**, 102002 (2002).
  - [12] Estabrook, F. B., Armstrong, J. W., Tinto, M., & Folkner, W. *Phys. Rev. D*, in press (2003) (gr-qc/0306071)
  - [13] LISA Study Team, *LISA: Laser Interferometer Space Antenna for the detection and observation of gravitational waves, Pre-Phase A Report*, 2nd ed. (Max Planck Institut für Quantenoptik, Garching, Germany, 1998).
  - [14] Peterseim, M. Robertson, D. I., Danzmann, K., Welling, H., & Bender, P., *Adv. Space Res.*, **25**, 1143 (2000).
  - [15] David Summers, "Algorithm tradeoffs," oral presentation, 3rd progress meeting of the ESA funded LISA PMS Project. ESTEC, NL, February 2003.
  - [16] Jenkins, G. M. & Watts, D. G. 1969, *Spectral Analysis and Its Applications*, (Holden Day: San Francisco)
  - [17] Tinto, M., Estabrook, F. B., & Armstrong, J. W., submitted to *Phys. Rev. D* (2003) (gr-qc/0310017)
  - [18] Prince, T. A., Tinto, M., Larson, S. L., and Armstrong, J. W. *Phys. Rev. D*, **66**, 122002 (2002)
  - [19] Tinto, M., Shaddock, D. A., Sylvestre, J. & Armstrong, J. W. accepted for publication in *Phys. Rev. D*, (2003) (gr-qc/0303013).
  - [20] Armstrong, J. W., Estabrook, F. B., & Tinto, M. *Classical Quantum Grav.*, **20**, S264 (2003)
  - [21] Królak, A., Tinto, M., and Vallisneri, M., in preparation (2003).
  - [22] Estabrook, F. B., and Wahlquist, H. D., *Gen. Rel. Grav.* **6**, 439 (1975); Wahlquist, H. D., *Gen. Rel. Grav.* **19**, 1101 (1987).
  - [23] <http://www.physics.montana.edu/lisa>, Version 2.0; Cornish, N. J. and Rubbo, L. J. *Phys. Rev. D* **67**, 022001 (2001)